

Cubic-scaling all-electron GW calculations with a separable density-fitting space-time approach

Ivan Duchemin^{*,†} and Xavier Blase[‡]

[†]*Univ. Grenoble Alpes, CEA, IRIG-MEM-L_Sim, 38054 Grenoble, France*

[‡]*Univ. Grenoble Alpes, CNRS, Inst NEEL, F-38042 Grenoble, France*

E-mail: ivan.duchemin@cea.fr

Abstract

We present an implementation of the GW space-time approach that allows cubic-scaling all-electron calculations with standard Gaussian basis sets without exploiting any localization nor sparsity considerations. The independent-electron susceptibility is constructed in a time representation over a non-uniform distribution of real-space locations $\{\mathbf{r}_k\}$ optimized within a separable resolution-of-the-identity framework to reproduce standard Coulomb-fitting calculations with meV accuracy. The compactness of the obtained $\{\mathbf{r}_k\}$ distribution leads to a crossover with the standard Coulomb-fitting scheme for system sizes below a few hundred electrons. The needed analytic continuation follows a recent approach that requires the continuation of the screened Coulomb potential rather than the much more structured self-energy. The present scheme is benchmarked over large molecular sets and scaling properties are demonstrated on a family of defected hexagonal boron-nitride flakes containing up to 6000 electrons.

1 Introduction

The GW approximation¹⁻¹¹ to the exchange-correlation self-energy has become a standard approach in solid-state physics to explore the electronic properties of metallic or semiconducting materials. Its accuracy was indeed proven superior to standard DFT calculations relying on the Kohn-Sham *ansatz* for the electronic energy levels (for large benchmark calculations on inorganic crystals, see e.g. Refs. 12,13). Further, following early applications in the late 90s,¹⁴⁻¹⁶ the GW formalism is nowadays widely used as well for the study of gas phase or dense ordered or disordered organic molecular systems.¹⁷⁻⁵⁶ The development of codes exploiting standard Gaussian atomic basis sets allowed in particular the comparison of all-electron GW calculations with higher level quantum-chemistry techniques (e.g. coupled-cluster) performed with the very same running parameters (geometry, atomic basis sets, resolution-of-the-identity, etc.)^{28,35,39,41}

The scaling of the number of operations needed to perform GW calculations with respect to the system size is typically $\mathcal{O}(N^4)$ within traditional planewave implementations. This scaling can be preserved with localized basis sets provided that resolution-of-the-identity (RI) techniques⁵⁷⁻⁶³ are used to avoid calculating response functions, such as the susceptibility, in the product space associated with valence-to-virtual molecular orbital products. While such a moderate scaling already allows calculations on systems containing well over a hundred atoms on supercomputers,⁶⁴⁻⁶⁷ attempts to deliver GW calculations with a lower scaling appeared with the seminal space-time approach by Rojas, Needs, Godby in 1995⁶⁸ and are now blooming.^{24,42,69-76}

This space-time formalism⁶⁸ stands as the first cubic-scaling GW approach relying on the separability of the independent-electron susceptibility χ_0 as the product of two Green's functions when expressed over a real-space grid, adopting further a time representation. This factorisation allows decoupling the summation over occupied and virtual molecular orbital contributions, leading to a cubic scaling scheme instead of the traditional quartic scaling calculation of χ_0 . Such a reduced scaling does not rely on any localization nor

sparsity considerations associated with e.g. 3-center integrals within the local direct overlap metric^{24,71,75} or a range-truncated Coulomb metric.⁷⁶

The imaginary-time formulation at the heart of the GW space-time approach is identical to the Laplace transform idea already in use in quantum chemistry for e.g. MP2 calculations.^{77,78} On the contrary, the use of a real space-grid was more naturally rooted in the pseudopotential planewave community, allowing by Fourier transform of the planewave basis to obtain relatively sparse uniform real-space grids. The space-time GW approach was more recently adapted to a full potential projector-augmented wave methodology,⁷⁰ building on an earlier application to calculating RPA correlation energies with cubic scaling.⁷⁹

In the case of all-electron calculations, the size of the real-space grid may seem an *a priori* bottleneck. However, real-space quadrature strategies have been already developed with much success in quantum chemistry for accelerating the calculation of 2-electron Coulomb integrals, including the chain-of-sphere (COSX) semi-numerical approach to exchange integrals⁸⁰⁻⁸² or the general tensor hypercontraction mathematical framework in its specific least-square grid optimization implementation (LS-THC).⁸³⁻⁸⁵ More recently, the interpolative separable density fitting (ISDF) approach^{86,87} represents a versatile strategy to combine the standard quantum chemistry resolution-of-the-identity (RI) techniques with a separable representation of the coefficients of molecular orbital products over auxiliary basis sets. The ISDF approach is now developing in the pseudopotential planewave or real-space grid community,^{72,88-91} including a recent GW implementation.⁷² Similarly, building on the expertise with resolution-of-the-identity (RI) techniques and/or real-space quadratures for Coulomb integrals, the ISDF scheme is also being explored by the quantum chemistry community working with localized (e.g. Gaussian) basis sets for explicitly correlated all-electron calculations such as QMC or Möller-Plesset techniques.^{92,93}

In a recent study, we presented an alternative to the ISDF formalism applied to all-electron Hartree-Fock, MP2 and RPA calculations with Gaussian basis sets.⁹⁴ In this scheme, standard auxiliary $\{P_\mu\}$ basis sets (e.g. cc-pVXZ-RI⁹⁵ or def2-XZVP-RI⁹⁶) are provided as

an input, as in any standard resolution-of-the-identity (RI) calculation, but the fitting procedure takes as an intermediate the expression of wave function and densities over compact non-uniform real-space grids $\{\mathbf{r}_k\}$. The corresponding fitting weights result from solving a quadrature equation that aims at reproducing the results of a standard Coulomb-fitting (RI-V) calculation. Adopting the space-time approach, cubic-scaling calculations of the independent-electron susceptibility at imaginary frequencies, and resulting RPA correlation energy, could be achieved. As compared to the corresponding RI-V calculation, an accuracy of a few $\mu\text{Hartree}/\text{electron}$ was demonstrated for RPA correlation energies with $\{\mathbf{r}_k\}$ distributions typically 4 times larger than the input auxiliary basis, allowing a crossover with the standard quartic-scaling RI-V RPA calculations for systems of the size of pentacene.

In the present work, we extend this formalism to all-electron cubic-scaling *GW* calculations. In contrast with the RPA formalism, where only imaginary-frequency susceptibilities are needed, we further exploit a recently developed^{97,98} analytic continuation scheme that brings to the real-frequency axis the dynamically screened Coulomb potential W rather than the much more structured *GW* self-energy. As compared to standard RI-V *GW* calculations, we demonstrate an accuracy at the meV level for the quasiparticle energies of large molecular sets. Finally, cubic scaling is evidenced using a family of defected hexagonal boron-nitride flakes with increasing radius containing up to 6000 electrons, with a crossover with the standard quartic scaling RI-V *GW* calculations for systems containing a very few hundred electrons.

2 Theory

2.1 The *GW* formalism with resolution-of-the-identity

We start by describing the standard resolution-of-the-identity (RI) framework for *GW* calculations. A more detailed discussion on RI techniques applied to MBPT can be found in Ref. 62. We just recall here that the essence of RI approximations, developed in particular to

tackle the calculation of 2-electron 4-center Coulomb integrals with localized atomic orbital (AO) basis sets,⁵⁷⁻⁶³ amounts to expressing the product of 2 molecular orbitals (MOs) over an auxiliary basis set $\{P_\mu\}$, namely:

$$\phi_n(\mathbf{r})\phi_m(\mathbf{r}) = \sum_{\mu} \mathcal{F}_{\mu}(\phi_n\phi_m)P_{\mu}(\mathbf{r}) \quad (1)$$

where we work with finite size systems allowing real molecular orbitals. For localized atomic-orbitals (AO) basis calculations, the auxiliary basis is typically 2-3 times larger than the AO basis set used to expand the MOs. As an example, the accurate RI-V Coulomb-fitting approach⁶⁰ defines the coefficients \mathcal{F}_{μ} as:

$$\mathcal{F}_{\mu}^V(\phi_n\phi_m) = \sum_{\nu} [V^{-1}]_{\mu\nu}(P_{\nu}|\phi_n\phi_m) \quad (2)$$

with $(P_{\nu}|\phi_n\phi_m)$ the 3-center Coulomb integrals

$$(P_{\nu}|\phi_n\phi_m) = \int d\mathbf{r}d\mathbf{r}' \frac{P_{\nu}(\mathbf{r})\phi_n(\mathbf{r}')\phi_m(\mathbf{r}')}{|\mathbf{r} - \mathbf{r}'|}$$

and $V_{\mu\nu}$ the Coulomb matrix elements in the auxiliary basis. Coming now to the *GW* formalism, we start with the expression of the independent-electron susceptibility along the imaginary-frequency axis:

$$\chi_0(\mathbf{r}, \mathbf{r}'; i\omega) = 2 \sum_{ja} \frac{\phi_j^*(\mathbf{r})\phi_a(\mathbf{r})\phi_a^*(\mathbf{r}')\phi_j(\mathbf{r}')}{i\omega - (\varepsilon_a - \varepsilon_j)} + c.c. \quad (3)$$

where (j) and (a) index occupied and virtual molecular orbitals (MOs), respectively, and where the factor (2) indicates a closed shell system. Expanding MO products over an auxiliary basis in the case of real-valued MOs leads to:

$$\chi_0(\mathbf{r}, \mathbf{r}'; i\omega) = \sum_{\mu\nu} P_{\mu}(\mathbf{r}) \cdot [\chi_0^{RI}(i\omega)]_{\mu\nu} \cdot P_{\nu}(\mathbf{r}') \quad (4)$$

with

$$[\chi_0^{RI}(i\omega)]_{\mu\nu} = 2 \sum_{ja} \frac{\mathcal{F}_\mu(\phi_j\phi_a)\mathcal{F}_\nu(\phi_j\phi_a)}{i\omega - (\varepsilon_a - \varepsilon_j)} + c.c. \quad (5)$$

In the standard RI framework, it is the quantity $[\chi_0^{RI}(i\omega)]_{\mu\nu}$ that is calculated in the auxiliary $\{P_\mu\}$ basis. The following steps start with the definition of the GW correlation self-energy as a convoluted integral along the real-energy axis

$$\Sigma^C(\mathbf{r}, \mathbf{r}'; E) = \frac{i}{2\pi} \int_{-\infty}^{\infty} d\omega e^{i\omega 0^+} G(\mathbf{r}, \mathbf{r}'; E + \omega) \widetilde{W}(\mathbf{r}, \mathbf{r}'; \omega) \quad (6)$$

with $\widetilde{W} = (W - V)$ and where G , W and V are the time-ordered 1-body Green's function, the screened and bare Coulomb potentials, respectively. In the contour-deformation approach,^{4,5} this expression is transformed into an integral along the imaginary-energy axis, plus the contribution of a few residues involving the screened Coulomb potential W calculated at real energies:

$$\begin{aligned} \Sigma_C^{GW}(\mathbf{r}, \mathbf{r}'; E) &= \frac{-1}{2\pi} \int_{-\infty}^{\infty} d\omega G(\mathbf{r}, \mathbf{r}'; E + i\omega) \widetilde{W}(\mathbf{r}, \mathbf{r}'; i\omega) \\ &\quad - \sum_i \phi_i(\mathbf{r})\phi_i(\mathbf{r}') \widetilde{W}(\mathbf{r}, \mathbf{r}'; \varepsilon_i - E) \theta(\varepsilon_i - E) \\ &\quad + \sum_a \phi_a(\mathbf{r})\phi_a(\mathbf{r}') \widetilde{W}(\mathbf{r}, \mathbf{r}'; E - \varepsilon_a) \theta(E - \varepsilon_a) \end{aligned} \quad (7)$$

Expressing the Green's function in a quasiparticle form

$$G(\mathbf{r}, \mathbf{r}'; i\omega) = \sum_n \frac{\phi_n(\mathbf{r})\phi_n(\mathbf{r}')}{i\omega - \varepsilon_n + i\eta \times \text{sgn}(\varepsilon_n - \mu)} \quad (8)$$

with $\eta = 0^+$ and μ the chemical potential, it appears that the expectation value of the GW correlation self-energy $\langle \phi_n | \Sigma_C^{GW} | \phi_n \rangle$ operator only requires integrals of the kind:

$$\langle \phi_n \phi_m | W(z) | \phi_n \phi_m \rangle = \sum_{\mu\nu} \mathcal{F}_\mu(\phi_m \phi_n) \mathcal{F}_\nu(\phi_m \phi_n) \langle P_\mu | W(z) | P_\nu \rangle \quad (9)$$

with z along the imaginary or real-energy axes. The needed $\langle P_\mu|W(z)|P_\nu\rangle$ matrix elements of the screened Coulomb potential are obtained from a Dyson-like equation projected into the auxiliary basis

$$\langle P_\mu|W(z)|P_\nu\rangle = \langle P_\mu|V|P_\nu\rangle + \sum_{\zeta\rho} \langle P_\mu|V|P_\zeta\rangle \cdot [\chi_0^{RI}(z)]_{\zeta\rho} \cdot \langle P_\rho|W(z)|P_\nu\rangle \quad (10)$$

where the random phase approximation (RPA) approximation is used.

2.2 The space-time approach from a separable resolution-of-identity framework

With the size of the auxiliary basis scaling linearly with system size, straightforward calculation of the $[\chi_0^{RI}(i\omega)]_{\mu\nu}$ matrix elements from equation 5 requires $\mathcal{O}(N^4)$ steps. In other words, for each (P_μ, P_ν) pair a double summation over occupied and unoccupied MOs is required. Following Almlöf and Häser,^{77,78} the Laplace transform:

$$\frac{1}{i\omega - (\varepsilon_a - \varepsilon_j)} + c.c. = -2 \int_0^{+\infty} d\tau \cos(\omega\tau) e^{-(\varepsilon_a - \varepsilon_j)\tau} \quad (11)$$

where the time integral converges since $(\varepsilon_j - \varepsilon_a) < 0$, allows to disentangle occupied and virtual energy levels in the denominator, leading to an imaginary time formulation

$$[\chi_0^{RI}(i\tau)]_{\mu\nu} = -2i \sum_{ja} \mathcal{F}_\mu(\phi_j\phi_a) \mathcal{F}_\nu(\phi_j\phi_a) e^{\varepsilon_j\tau} e^{-\varepsilon_a\tau} \quad (12)$$

where the (i) factor is introduced to match the standard definition of the independent-electron susceptibility in the time domain. However, occupied and virtual MOs are still entangled in the $\mathcal{F}_{\mu/\nu}(\phi_j\phi_a)$ weight factors. This is precisely the goal of the separable RI

introduced in Ref. 94 in the context of RPA total energies, with the expansion :

$$\mathcal{F}_\mu^{RS}(\phi_j\phi_a) = \sum_k M_{\mu k} \phi_j(\mathbf{r}_k)\phi_a(\mathbf{r}_k) \quad (13)$$

where the ϕ_j and ϕ_a MOs are factorized, leading to the wording separable-RI that we label RI-RS where RS stands for real-space. The present scheme targets a standard calculation with input molecular orbitals (MO) Gaussian basis and its associated auxiliary basis sets, and the $\{\mathbf{r}_k\}$ distribution is an intermediate representation designed to reproduce the accuracy of a standard Coulomb-fitting calculation with the input basis sets. This is described here below and in Ref. 94 for Hartre-Fock, RPA and MP2 calculations.

The separable real-space RI (RI-RS) leads to expressing the independent-electron susceptibility matrix elements in the auxiliary basis as

$$[\chi_0(i\tau)]_{\mu\nu} \stackrel{RI-RS}{=} \sum_{kk'} M_{\mu k} \cdot \chi_0(\mathbf{r}_k, \mathbf{r}_{k'}; i\tau) \cdot M_{\nu k'} \quad (14)$$

where for any $(\mathbf{r}, \mathbf{r}')$ pair of points in real-space

$$\chi_0(\mathbf{r}, \mathbf{r}'; i\tau) = -iG(\mathbf{r}, \mathbf{r}'; i\tau)G(\mathbf{r}', \mathbf{r}; -i\tau) \quad (15)$$

$$G(\mathbf{r}, \mathbf{r}'; i\tau) = i \sum_j^{\text{occ}} \phi_j(\mathbf{r})\phi_j(\mathbf{r}')e^{\varepsilon_j\tau} \quad (\tau > 0) \quad (16)$$

$$= -i \sum_a^{\text{vir}} \phi_a(\mathbf{r})\phi_a(\mathbf{r}')e^{\varepsilon_a\tau} \quad (\tau < 0) \quad (17)$$

where G is the time-ordered one-body Green's function. Considering here that the MOs are spin-orbitals, one can recover the factor two in Equation 12 for spin-restricted systems. Eq. 15 is the standard equation for the original space-time approach⁶⁸ with the summations over occupied and virtual MOs completely decoupled, leading to a strictly cubic-scaling number of operations, independently of any localization nor sparsity properties. After construction of the imaginary-time independent-electron susceptibility in the $\{P_\mu\}$ Gaussian auxiliary basis

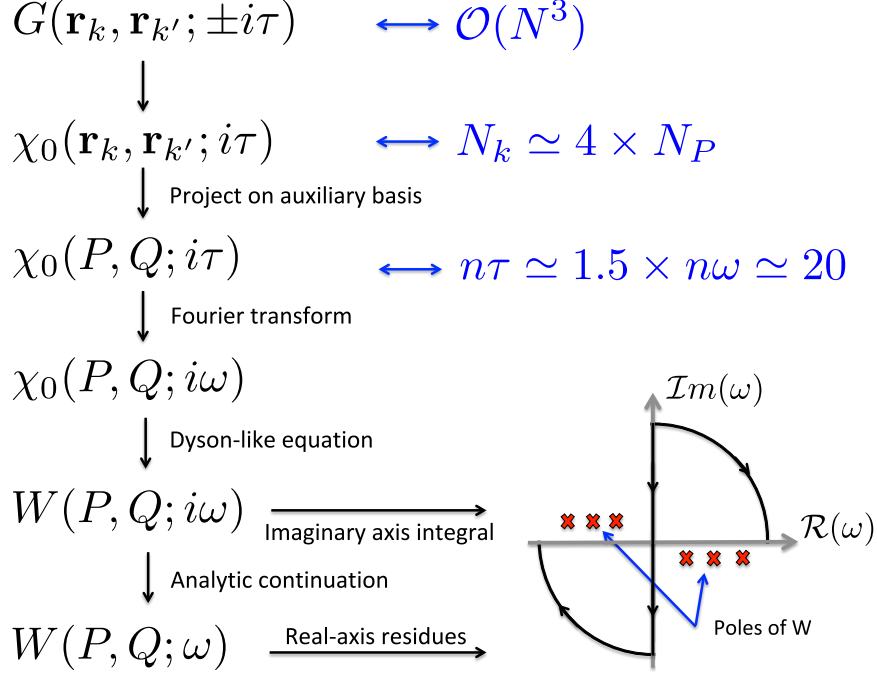


Figure 1: Schematic representation of the steps involved in the present cubic scaling all-electron space-time approach. The optimized set of real-space positions $\{\mathbf{r}_k\}$ is typically 4 times as large as the corresponding input Gaussian auxiliary basis $\{P_\mu\}$. The number of imaginary times and frequencies is set by $n\tau$ and $n\omega$. In the contour deformation approach (see Inset) only the screened Coulomb potential W needs to be continued from the imaginary to the real-energy axis, avoiding the continuation of the much more structured self-energy (see Ref. 98).

following Eq. 14, the $[\chi_0^{RI}(i\omega)]_{\mu\nu}$ are obtained by Fourier transform at imaginary frequencies. Following Eq. 10, the screened Coulomb potential $\langle P_\mu | W(z) | P_\nu \rangle$ is finally obtained along the imaginary frequency axis. Details about the time and frequency grids will be given below when discussing the analytic continuation of W to the real-axis. The overall flow of calculations is presented in Fig. 1. While we use in the present scheme the analytic continuation of W , the standard analytic continuation of Σ to the real axis can also be used once the $\chi_0(P, Q; i\omega)$ susceptibilities are obtained using the real-space imaginary-time approach.

2.3 Construction of the $\{\mathbf{r}_k\}$ distributions

A crucial aspect of the present scheme is the size of the $\{\mathbf{r}_k\}$ -set that controls the prefactor associated with the present cubic-scaling scheme. Following our implementation of cubic-scaling RPA calculations in an all-electron space-time approach,⁹⁴ the central idea is not to use a generic real-space grid (such as Becke grids⁹⁹ adopted to express densities in DFT codes) but to optimize for each atomic species a reduced set of $\{\mathbf{r}_k\}$ points sufficient to reach the *accuracy of the standard Coulomb-fitting RI-V approximation* in conjunction with the chosen auxiliary basis set. Such task is performed by minimizing the difference between the \mathcal{F}^{RS} and \mathcal{F}^V fitting procedure as defined in Eqs. 2 and 13, in the Coulomb norm sense, and taking into account all MO products of a single atom of the species considered. As introduced in Ref. 94, the $M_{\mu k}$ coefficients are fixed through a linear least square equation, and thus only the $\{\mathbf{r}_k\}$ -sets are considered as optimization variables. The global minimization process thus writes

$$\operatorname{argmin}_{\{\mathbf{r}_k\}} \sum_{\mu\alpha\alpha'} \left| (\mathcal{F}_\mu^{RS}(\alpha\alpha') - \mathcal{F}_\mu^V(\alpha\alpha')) P_\mu \right|_V^2 \quad (18)$$

where the $\{\alpha\}$ are the Gaussian basis functions used to expand the MOs.

For a given atom, the initial set of points are constructed as a superposition of high symmetry subsets of Lebedev grids up to order 9, associated with different sphere radii (see Supporting Information Ref. 94). The optimization process starts by minimizing the penalty function of Eq. 18 adjusting first the radii. This is similar to the optimization strategy adopted in the grid-based formulation of LS-THC⁸⁵ but fitting the codensities coefficients rather than the 4-center Coulomb integrals. In a second step, all constraints are raised and every point is allowed to move independently. This non-linear minimization process is performed using a basin-hopping mechanism coupled to a L-BFGS (limited memory Broyden-Fletcher-Goldfarb-Shanno) algorithm. We emphasize that such a step is done once for all for a given element and the chosen basis sets. Experimenting with such a strategy for the def2-TZVP / def2-TZVP-RI associated basis sets leads to 100 $\{\mathbf{r}_k\}$ points for H and

He, and 336, 436 and 536 points for elements in the second, third, and fourth row of the periodic table, respectively. Such grid sizes allow an agreement at the meV level between subsequent quasiparticle energies calculated with the present real-space approach and the standard Coulomb-fitting RI-V scheme. Except for the first row, this is typically 3.5 to 4.5 times larger than the number of elements in the def2-TZVP-RI set. Better optimization schemes and reducing the initial number of Lebedev subsets may lead to reduce these $\{\mathbf{r}_k\}$ distribution sizes. However, as shown below, the present approach already provides an excellent accuracy-to-cost ratio and appears to be very robust, with no outliers as tested over large molecular sets.

In a second step, the $\{\mathbf{r}_k\}$ distribution for the molecular system is built as the superposition of the isolated atoms $\{\mathbf{r}_k\}$ distributions and only the weights $\{M_{\mu k}\}$, as defined in Eq. 13, need to be calculated for each considered molecular system. Such a step only requires $\mathcal{O}(N^3)$ operations since the least-square estimator matrix $[M]_{\mu k}$ is obtained in a matrix multiplication/inversion formulation from the target \mathcal{F}_μ^V coefficients (see Ref. 94). As such, the weights $\{M_{\mu k}\}$ are univocally defined once the $\{\mathbf{r}_k\}$ grid and \mathcal{F}_μ^V factors are set-up. We provide in the Supporting Information a graph confirming the cubic-scaling of the $\{M_{\mu k}\}$ construction that amounts to about 25% of the total CPU time, including the calculation of the target \mathcal{F}_μ^V , for non-self-consistent G_0W_0 calculations. This 2-step process, namely the optimization of the $\{\mathbf{r}_k\}$ -distribution on isolated atoms, dramatically simplifies the minimization process while preserving excellent accuracy as demonstrated below.

Concerning previous RPA calculations using the present separable RI with Laplace transform scheme,⁹⁴ the crucial observation was that indeed $\{\mathbf{r}_k\}$ -sets typically 4 times larger than the used auxiliary $\{P_\mu\}$ basis set were sufficient to reproduce the accuracy of standard RI-V calculations to within a few μ Hartree/electron for the exchange, RPA and MP2 total energies. Namely, replacing the standard RI-V \mathcal{F}_μ^V coefficients by their \mathcal{F}_μ^{RS} approximants preserved an excellent accuracy, with a number of points sufficiently small to offer a crossover with the standard quartic-scaling RI-V RPA approach for systems of the size of pentacene.

We will perform here below the corresponding accuracy check for the quantity of interest here, namely the *GW* quasiparticle energies, showing that meV accuracy can be achieved with a crossover between the present separable RI-RS scheme and standard RI-V calculations for systems containing less than a few hundred electrons. This crossover is independent of the compactness and dimensionality of the studied systems since sparsity and localization are not exploited.

2.4 Analytic continuation, frequency and time grids

An important aspect of the space-time approach is the required analytic continuation from the imaginary to the real-frequency axis. With the calculation of the susceptibility $\chi_0(i\tau)$ at imaginary times, the imaginary-frequency $\chi_0(i\omega)$ analog can be obtained by Fourier transform. From such quantities, the screened Coulomb potential $W(i\omega)$ and self-energy $\Sigma(i\omega)$ can be obtained at imaginary frequencies and efficiently continued analytically to the real energy axis as performed in many codes.

An alternative to the analytic continuation of the self-energy was proposed by Christoph Friedrich in the context of *GT* calculations on solid iron,⁹⁷ and by ourselves in the present case of *GW* calculations on molecular systems with extensive benchmark accuracy checks.⁹⁸ The central idea is to adopt the contour deformation scheme where the quantity needed along the real-axis is no longer the self-energy directly, but the screened Coulomb potential (see second and third lines of Eq. 7). Since the self-energy contains $(N_W \times N_G)$ poles, where N_G and N_W are respectively the number of poles of the Green's function and screened Coulomb potential, the screened Coulomb potential is much less structured than the self-energy itself, leading to a much more robust analytic-continuation scheme. Difficult test cases drawn from the *GW100* test sets,³⁶ such as the *MgO* or *BN* dimers, were shown to be very accurately treated with the calculations of the screened Coulomb potential $W(i\omega)$ for no more than 12 frequencies along the imaginary-axis. In particular, these frequencies are constructed so as to minimize the error over the imaginary axis integration contribution to Equation 7. We

address the reader to Ref. 98 for a detailed presentation of this scheme. We keep the number of imaginary frequencies to $n\omega=12$ that was shown in this former study to lead to sub-meV accuracy, as compared to the contour deformation scheme, for GW calculations on frontier orbitals using this “robust” analytic continuation scheme.

Table 1: Acridine def2-TZVP $G_0W_0@PBE0$ HOMO and LUMO (in eV) convergence against the imaginary frequency grid size. We keep the ratio $n\tau = 1.5 \times n\omega$. The real-space with Laplace transform (RI-RS + LT) depends on both frequency and time grids. All calculations are performed with the auxiliary def2-TZVP-RI basis set, while RI-RS calculations use an extra $\{\mathbf{r}_k\}$ distribution optimized for the corresponding def2-TZVP/def2-TZVP-RI basis sets association.

$n\omega$	RI-V	RI-RS	RI-RS + LT
HOMO			
6	-7.55777	-7.55777	-7.55787
8	-7.56073	-7.56072	-7.56071
10	-7.56113	-7.56112	-7.56112
12	-7.56112	-7.56111	-7.56111
14	-7.56112	-7.56111	- -
LUMO			
6	-0.75723	-0.75719	-0.75713
8	-0.76020	-0.76016	-0.76018
10	-0.76046	-0.76042	-0.76042
12	-0.76044	-0.76040	-0.76040
14	-0.76044	-0.76040	- -

Once the imaginary frequencies are set, the corresponding imaginary-time grid is constructed following Ref. 94, where the present space-time approach was explored for RPA total energy calculations. The selected times $\{\tau_p, p = 1, n\tau\}$ are optimized for the chosen set of imaginary frequencies z_k ($k=1, n\omega$) through the minimization process:

$$\arg \min_{\omega_k^p, \tau_p} \left[\sum_k \int_{\ln(E_{min})}^{\ln(E_{max})} du \left| \sum_p \omega_k^p e^{-\tau_p e^u} - \left[\frac{1}{e^u + iz_k} - \frac{1}{e^u - iz_k} \right] \right|^2 \right] \quad (19)$$

where ω_k^p is the weight associated with a given τ_p time for a targeted z_k frequency. The energies E_{min} and E_{max} are the energy gap and the maximum ($\varepsilon_a - \varepsilon_i$) value, respectively. The $1/(e^u \pm iz_k)$ factors represent the pole structure of the independent-electron susceptibility

along the imaginary axis. The $\sum_p \omega_k^p e^{-\tau_p e^u}$ approximant translates the fact that $e^{-a|\tau|}$ ($a > 0$) is the Fourier transform of $2a/(a^2 + \omega^2)$ within a prefactor. Following Refs. 94,98, the log scale is used so as to allow a regular sampling of the error oscillations at energies between E_{min} and E_{max} . The problem can be then solved in a traditional least square approach using a uniform sampling in u . Such a formulation conserves an excellent accuracy, as demonstrated in Table 1, with a number of grid points comparable to that commonly adopted with the more elaborated minimax approach.^{70,79,100} Similarly to the minimax formulation, the grids points τ_p have been pre-tabulated with the E_{max}/E_{min} ratio as a single parameter, so as to minimize the computational effort of the setup. On the other hand, the ω_k^p coefficients can be conveniently recalculated on the fly as the result of a simple linear least square equation. In association with $n\omega=12$ imaginary frequencies, $n\tau=18$ times are selected to reach sub-meV accuracy on the quasiparticle energies. We provide in Table 1 a typical test of accuracy, selecting the def2-TZVP $G_0W_0@PBE0$ HOMO and LUMO energies of acridine, the first element of the molecular set of Ref. 41 studied in full details in the next section. In this Table, RI-RS without Laplace transform only differs from the standard Coulomb-fitting (RI-V) by the construction of the \mathcal{F}_μ fitting coefficients. We observe in particular that the dependence on the $n\omega$ grid falls well below the meV for $n\omega \geq 10$. The real-space approach with Laplace-transform (RI-RS+LT) depends further on the imaginary-time grid. However, for a given $n\omega$ imaginary-frequency grid, a time-grid with $n\tau = 1.5 \times n\omega$ introduces negligible errors, comforting overall our choice of $n\omega = 12$ and $n\tau=18$ running parameters.

3 Results

3.1 Validation and accuracy

We benchmark the accuracy of the present scheme using the recent set of 24 intermediate size molecules with acceptor character proposed in Ref. 41. Our calculations are performed at the def2-TZVP $G_0W_0@PBE0$ level associated with the corresponding def2-TZVP-RI auxiliary

basis.⁹⁶ Our goal here is not to carry calculations in the complete-basis set limit, but rather to assess the accuracy of the present space-time approach, as compared to the standard Coulomb-fitting (RI-V) scheme, using a reasonable basis set. The real-space $\{\mathbf{r}_k\}$ sets were thus optimized for the def2-TZVP and def2-TZVP-RI basis sets association, following the scheme described above and summarized in Eqn. 18. As discussed above, the size of the $\{\mathbf{r}_k\}$ atomic distributions amounts to 136 for H and 336 for second row elements.

We provide in Table 2 the def2-TZVP G_0W_0 @PBE0 highest occupied (HOMO) and lowest unoccupied (LUMO) molecular orbitals energies calculated using the standard Coulomb-fitting (RI-V) scheme and the separable real-space (RI-RS) approach in conjunction with the Laplace transform scheme. Both calculations are performed with the “robust” analytic continuation (AC) scheme.⁹⁸ Direct contour-deformation calculations without any analytic continuation, namely calculating directly the needed residues of W along the real-axis within the standard quartic scaling RI-V formalism, shows that the errors introduced by the AC are well below the meV for the HOMO and LUMO energy levels of the molecules contained in this set. The analysis of the results evidences that for such $\{\mathbf{r}_K\}$ distributions, the error on the quasiparticle energies remains below the meV. Such an accuracy may be tuned by increasing/decreasing the size of the $\{\mathbf{r}_k\}$ distributions, but the present accuracy-to-size trade-off is already excellent in practice.

We further perform benchmark def2-TZVP G_0W_0 @PBE0 calculations on the $GW100$ test set^{35,36,43,47,72,98,101} that contains elements from the third and fourth periods of the periodic table, including transition metal complexes. We exclude the 5 systems containing 5-th period elements for which the def2-TZVP basis set requires the use of an effective core potential, namely Xe, Rb₂, I₂, vinyl iodide (C₂H₃I) and aluminum iodide (AlI₃). Similarly to the previous test set, the error induced by the real-space RI-RS with Laplace transform technique, as compared to a standard RI-V calculations, is below the meV for most molecules as reported in Fig. 2. Three systems (Kr, CuCN, SF₄) show an error on the HOMO slightly larger than 1 meV (in absolute value), while all errors on the LUMO value are below the

Table 2: HOMO and LUMO energies at the def2-TZVP G_0W_0 @PBE0 level for the molecular set of Ref. 41. Molecules are arranged by chemical families in the order of Ref. 41. The standard Coulomb-fitting scheme (RI-V) performed with the def2-TZVP-RI auxiliary basis set⁹⁶ is compared to the present real-space Laplace-transform (RI-RS) calculations. Negative and positive maximum errors, the mean absolute (MAE) and mean signed (MSE) errors are indicated in meV. Values leading to the largest error are in bold.

	HOMO		LUMO	
	RI-V [eV]	RI-RS [eV]	RI-V [eV]	RI-RS [eV]
anthracene	-7.0787	-7.0787	-0.4233	-0.4234
acridine	-7.5611	-7.5611	-0.7604	-0.7604
phenazine	-7.9755	-7.9754	-1.1796	-1.1799
azulene	-7.1271	-7.1272	-0.5595	-0.5597
benzoquinone (BQ)	-9.7275	-9.7273	-1.6004	-1.6006
naphthalenedione	-9.3297	-9.3296	-1.5520	-1.5521
dichlone	-9.4112	-9.4111	-1.9812	-1.9814
F4-BQ	-10.5855	-10.5853	-2.3221	-2.3220
Cl4-BQ	-9.7245	-9.7246	-2.5192	-2.5191
nitrobenzene	-9.7868	-9.7867	-0.5485	-0.5486
F4-benzenedicarbonitrile	-10.2336	-10.2334	-1.7207	-1.7210
dinitro-benzonitrile	-10.7596	-10.7595	-1.8683	-1.8684
nitro-benzonitrile	-10.2038	-10.2038	-1.3992	-1.3993
benzonitrile	-9.5108	-9.5107	0.1831	0.1828
fumaronitrile	-10.9712	-10.9710	-1.0740	-1.0740
mDCNB	-10.0173	-10.0175	-0.7227	-0.7228
TCNE	-11.4676	-11.4674	-3.2543	-3.2544
TCNQ	-9.1373	-9.1373	-3.5795	-3.5795
maleic-anhydride	-10.7783	-10.7782	-1.0029	-1.0031
phthalimide	-9.6757	-9.6755	-0.6380	-0.6381
phthalic-anhydride	-10.1111	-10.1111	-0.9060	-0.9061
Cl4-isobenzofuranedione	-9.5809	-9.5807	-1.7124	-1.7127
NDCA	-8.7061	-8.7058	-1.3302	-1.3304
BODIPY	-7.8008	-7.8008	-1.6315	-1.6316
Max. err.	+0.32 meV / -0.23 meV		+0.07 meV / -0.33 meV	
MAE	0.12 meV		0.14 meV	
MSE	0.08 meV		0.12 meV	

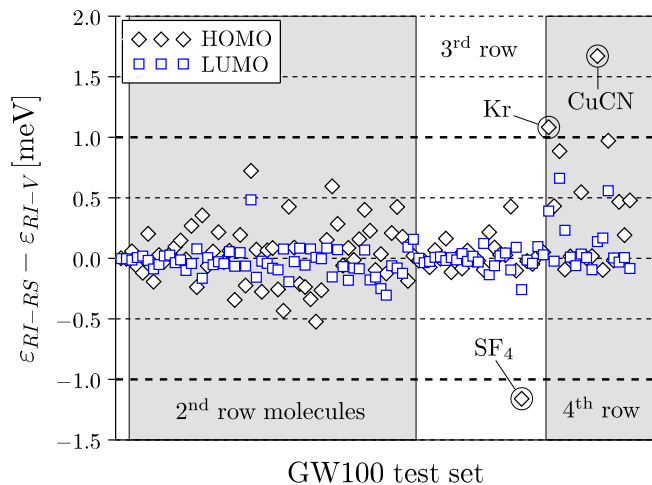


Figure 2: HOMO/LUMO def2-TZVP $G_0W_0@PBE$ quasi-particle energy discrepancy analysis over the $GW100$ test, excluding the 5 systems containing 5-th period elements (see text). The error is that of the present real-space Laplace-transform (RI-RS) approach with respect to the standard Coulomb-fitting (RI-V) approach performed with the corresponding def2-TZVP-RI auxiliary basis set.⁹⁶ The molecules of the set are sorted according to the maximum period (row) involved within the periodic table.

meV. As emphasized above, optimizing further the distribution of $\{\mathbf{r}_k\}$ points may bring all errors below the meV, but the purpose of the present study is to show that the present scheme, as it stands, already brings very consistently the error at the meV level. Overall, the mean absolute (MAE) errors amount to 0.21 meV and 0.09 meV for the HOMO/LUMO, respectively. All data can be found in the Supporting Information. The present data confirm, in the specific case of GW calculations, previous studies reporting on the excellent accuracy-to-cost ratio associated with grid-based techniques for the evaluation of exact exchange or explicit correlation energies in the context of all-electron atomic-orbital basis sets calculations.^{80–85,94,102,103}

3.2 Scaling analysis

We finally address the issue of scaling with respect to the system size through the example of finite-size hexagonal boron-nitride (h -BN) “flakes” containing a central point-defect. The

study of the optical emission mediated by defects in *h*-BN is an important technological research area, with the prospect of having at hand stable, room-temperature, polarized and ultrabright single-photon sources, together with a scientific challenge when it comes to identify the defects and mechanisms responsible for such sharp emission lines in the visible range.¹⁰⁴⁻¹⁰⁸

We select as a test case the $C_B V_N$ (nitrogen vacancy plus carbon substitution to neighbouring boron) defect that has been recently identified as a possible candidate for emission at about 2 eV.¹⁰⁹ Our goal here is not to confirm the likeliness of such a defect, but rather to start exploring whether many-body calculations with a typical defect can be performed using finite-size clusters, rather than the traditional supercell approach using periodic boundary conditions (PBC). Indeed, the use of PBC complicates the calculations of charged excitations due to the electrostatic interaction between cells, and the Coulomb potential must be truncated to avoid spurious contributions even in the limit of large supercells. As such, the modeling of the opto-electronic properties of defects in *h*-BN at the many-body *GW* and Bethe-Salpeter level remains scarce due in particular to the cost of performing the required large-scale *GW* calculations.^{109,110}

The edge of the *h*-BN flakes are passivated by hydrogen atoms to avoid dangling bonds and the HOMO-LUMO gap is clearly controlled by very localized defect states yielding energy levels within the gap of pristine *h*-BN (see Inset Fig. 3 for the LUMO). The size of the studied flakes correspond to average radii ranging from 21.5 to 56.4 Å, containing from 137 to 941 C, B or N atoms, that is from 167 to 1019 atoms including passivating H atoms. The average diameter is defined as $\bar{D} = 2\sqrt{N_{at}S_{at}/\pi}$, where N_{at} is the number of B or N atoms, and $S_{at} = 3\sqrt{3}d_{BN}^2/4$ is the effective surface per B or N atom in the hexagonal lattice, with d_{BN} the BN bond length. Structural relaxation at the PBE0 6-311G* level indicates that the ground-state for these systems is not spin-polarized.

Before discussing scaling properties, we briefly comment on the evolution of the HOMO-LUMO energy gap obtained at the 6-311G* $G_0W_0@PBE0$ level¹¹¹ as a function of system

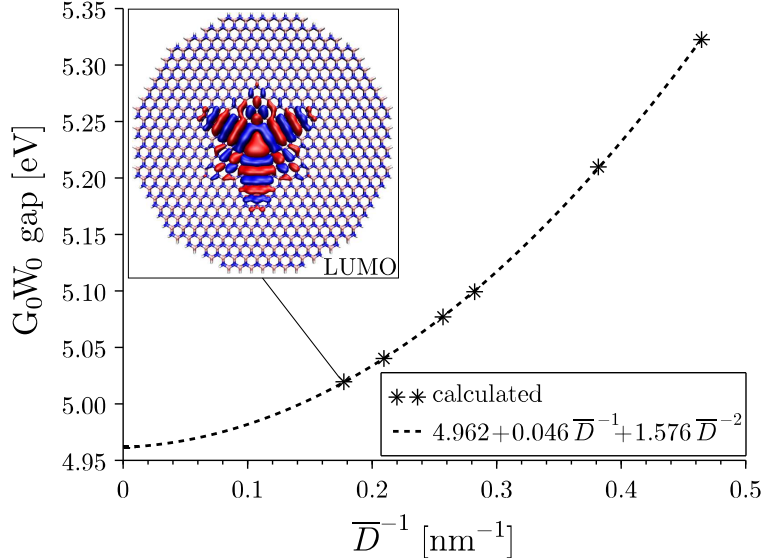


Figure 3: Plot of the 6-311G* $G_0W_0@PBE0$ HOMO-LUMO gap as a function of the inverse flake average diameter. The Inset represents the Kohn-Sham LUMO associated with our largest flake (1019 atoms).

size (see Fig. 3). Our goal here is not to obtain converged values with respect to basis completeness, but to study the evolution of the gap with system size using a minimal triple-zeta plus polarization basis, keeping in mind that the 6-311G* HOMO-LUMO gaps for our defected flakes are typically 70 meV larger than that obtained with the larger def2-TZVP basis set. The decrease of the gap with increasing diameter can be attributed to polarization effects, namely the fact that upon calculating the ionization potential or electronic affinity, as measured by a photo-emission experiment, the added charge localized on the defect generates a long-range Coulomb field that polarizes the surrounding atoms. Such a polarization, properly described within the GW formalism, stabilizes the added hole or electron, closing the gap. In the case of finite size systems, this polarization is incomplete as compared to an infinite sheet, leading to a HOMO-LUMO gap that is too large. Performing a fit of the GW gap up to second order in $(1/\overline{D})$, the linear contribution is found to be negligible, leading to a simple quadratic dependence. Such a quadratic behaviour stems from the reaction field generated by the 2D density of dipoles induced by a charge added or removed on/from the LUMO/HOMO levels.¹¹² The extrapolated gap at infinite radius amounts to 4.96 eV, still

$\simeq 60$ meV away from the gap of the largest flake studied. As expected, the G_0W_0 gap is much larger than the PBE0 Kohn-Sham gap of 3.07 eV obtained for the largest system. Fitting the data associated with the 4 smallest flakes, the extrapolated value remains within 20 meV of the extrapolated value with the fit containing all points. This indicates the stability of the extrapolation scheme and suggests that an accurate asymptotic value may be obtained with calculations performed on systems containing a rather limited number of atoms. While the isolated defect limit GW quasiparticle gap needs extrapolating to infinite sizes, preliminary results indicate that optical excitations, which are neutral excitations of the system, converge much faster as a function of system size.

We now plot (log scale) in Fig. 4 the total CPU time (namely the sum of all cores CPU time, over the complete run) associated with the G_0W_0 calculations reported in Fig. 3. We compare in particular the standard RI-V (Coulomb fitting) calculations (filled blue triangles) performed with the universal Coulomb fitting auxiliary basis of Ref. 113 and the present real-space Laplace-transform approach (filled black circles) with a real-space $\{\mathbf{r}_k\}$ distribution optimized as described above for this specific auxiliary basis set. Timings are reported in Tables S2 and S3 of the Supporting Information where the specific contributions from the RI-RS set-up, susceptibility calculations, Dyson-equation inversion and self-energy calculations are further provided.

These calculations confirm that the present space-time scheme offers a cubic scaling with system size (see black dot-dashed fit) with an (extrapolated) crossover with the standard quartic scaling RI-V scheme taking place for about 350 electrons. We further explore limit of small system sizes with a larger def2-TZVP basis associated with its def2-TZVP-RI auxiliary basis. We can see that despite the larger basis sets, the overhead of the 128 core distribution and pre-computation phases still hinders slightly the fit by perfect cubic/quartic lines in the small system size limit. Nonetheless, these later calculations confirms a crossover that consistently takes place at about 350 electrons ($\simeq 50-60$ B/N atoms). A similar crossover was observed in the case of cc-pVTZ RPA calculations where we used a similar real-space

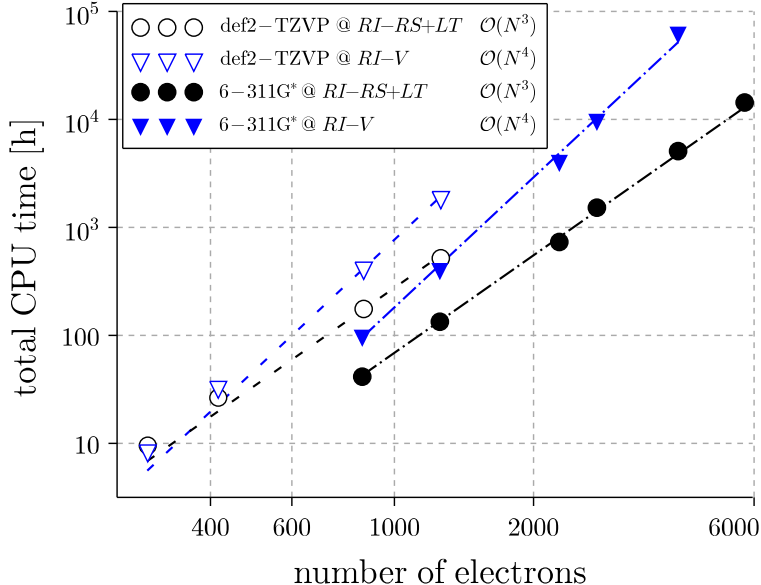


Figure 4: Scaling properties (log scale) for the standard Coulomb-fitting (RI-V) G_0W_0 calculations compared with the present real-space Laplace-transform (RI-RS+LT) scheme. Calculations have been performed with the def2-TZVP and 6-311G* basis sets. For the standard RI-V scheme, the auxiliary def2-TZVP-RI⁹⁶ and universal Coulomb fitting¹¹³ basis sets, respectively, were used. Calculations were performed on a set of hexagonal boron-nitride flakes with up to 6000 electrons. Calculations have been performed on AMD Rome Epyc nodes with 128 cores/node and 1.85 Gb/core. The black (RI-RS+LT) and blue (RI-V) dot-dashed lines are cubic and quartic fits, respectively. An unconstrained fit yields a scaling exponent of 3.07 for the (RI-RS+LT) scheme.

Laplace-transform approach to build the independent-electron susceptibility (see Ref. 94).

All calculations have been performed on a supercomputer built of 128 cores 2,6 GHz AMD Rome nodes with 1.85 Gb/core memory. We only used fully filled nodes in order to maintain consistency between the timings presented here, meaning that the smallest system calculations have been distributed on a minimum of 128 cores. Under this constraint, we selected CPU grid sizes that roughly match the minimum memory requirement for each calculation, as detailed in Table S2 of the Supporting Information. Our real-space Laplace-transform (RI-RS+LT) calculations require much less cores than the standard RI-V scheme, partly due to the corresponding $\mathcal{O}(N^2)$ memory footprint, with the $\chi_0(\mathbf{r}_k, \mathbf{r}'_k; i\omega)$ being the largest objects stored in memory. On the other hand, the memory requirement of our standard RI-V implementation grows as $\mathcal{O}(N^3)$, dominated in this case by the storage of

(occupied) \times (virtual) co-density auxiliary fits $\mathcal{F}_\mu^V(\phi_i\phi_a)$. Let us emphasize that within the RI-RS+LT approach, each 3-center integral is computed and immediately discarded during the RI setup.

4 Conclusions

We have presented an all-electron space-time GW formalism relying on a separable resolution-of-the-identity (RI) formalism, offering cubic-scaling GW calculations that do not exploit any sparsity nor localization considerations. This allows a crossover with the quartic scaling Coulomb-fitting RI-V GW calculations for systems containing a very few hundred electrons, independently of the dimensionality of the studied system. As compared to the interpolative separable density fitting (ISDF) scheme, the present approach preserves the use of standard auxiliary Gaussian basis sets that are taken as an input, and not constructed by the ISDF algorithm. The needed distribution of $\{\mathbf{r}_k\}$ points are optimized to recover at the meV level the results of a standard Coulomb-fitting (RI-V) GW calculation. Precalculated grids to be associated with a larger collection of standard basis sets, beyond the 6-311G* and def2-TZVP sets adopted in this study, comes now as a prerequisite for a broader use of the present scheme. Scaling with system size could be further reduced possibly by exploiting stochastic techniques⁶⁹ or the decay properties of the space-time Green's functions¹¹⁴ at long-range in the case of very large systems. The performances as they stand today clearly illustrate however the interest of real-space quadrature, as developed by the quantum chemistry community for all-electron atomic-orbital basis sets calculations, and the progress performed by the GW community to install this family of many-body perturbation techniques as a valuable tool for moderately correlated systems, with an excellent trade-off between accuracy and CPU time, allowing to tackle finite size or periodic systems, metallic or semiconducting, containing up to several hundred atoms.

Acknowledgement

The authors are indebted to Pascal Pochet for discussions concerning defects stability in periodic and finite size systems and to Gabriele D’Avino for explaining the quadratic behaviour of the polarization energy with inverse diameter. Calculations have been performed thanks to an allocation on the French CEA-TGCC Joliot-Curie supercomputer comprizing 2292 AMD Rome Epyc nodes with 128 cores/node and 2 Go/core. This work received support from the French *Agence Nationale de la Recherche* (ANR) under contract ANR-20-CE29-0005.

Supporting Information Available

We provide in the Supporting Information the details of the *GW*100 test set data (Table S1) and additional information about the systems size, timings and number of cores used for the 6-311G* G_0W_0 @PBE0 calculations on the hexagonal boron-nitride flakes (Tables S2-S3 and Fig. S1).

References

- (1) Hedin, L. New Method for Calculating the One-Particle Green’s Function with Application to the Electron-Gas Problem. *Phys. Rev.* **1965**, *139*, A796–A823.
- (2) Strinati, G.; Mattausch, H. J.; Hanke, W. Dynamical Correlation Effects on the Quasiparticle Bloch States of a Covalent Crystal. *Phys. Rev. Lett.* **1980**, *45*, 290–294.
- (3) Hybertsen, M. S.; Louie, S. G. Electron correlation in semiconductors and insulators: Band gaps and quasiparticle energies. *Phys. Rev. B* **1986**, *34*, 5390–5413.
- (4) Godby, R. W.; Schlüter, M.; Sham, L. J. Self-energy operators and exchange-correlation potentials in semiconductors. *Phys. Rev. B* **1988**, *37*, 10159–10175.

- (5) Farid, B.; Daling, R.; Lenstra, D.; van Haeringen, W. GW approach to the calculation of electron self-energies in semiconductors. *Phys. Rev. B* **1988**, *38*, 7530–7534.
- (6) Aryasetiawan, F.; Gunnarsson, O. The GW method. *Rep. Prog. Phys.* **1998**, *61*, 237–312.
- (7) Farid, B. In *Electron Correlation in the Solid State - Chapter 3*; March, N., Ed.; Imperial College Press, London, 1999.
- (8) Onida, G.; Reining, L.; Rubio, A. Electronic excitations: density-functional versus many-body Green's-function approaches. *Rev. Mod. Phys.* **2002**, *74*, 601–659.
- (9) Ping, Y.; Rocca, D.; Galli, G. Electronic excitations in light absorbers for photoelectrochemical energy conversion: first principles calculations based on many body perturbation theory. *Chem. Soc. Rev.* **2013**, *42*, 2437–2469.
- (10) Martin, R.; Reining, L.; Ceperley, D. *Interacting Electrons: Theory and Computational Approaches*; Cambridge University Press, 2016.
- (11) Golze, D.; Dvorak, M.; Rinke, P. The GW Compendium: A Practical Guide to Theoretical Photoemission Spectroscopy. *Front. Chem.* **2019**, *7*, 377.
- (12) van Schilfgaarde, M.; Kotani, T.; Faleev, S. Quasiparticle Self-Consistent GW Theory. *Phys. Rev. Lett.* **2006**, *96*, 226402.
- (13) Shishkin, M.; Marsman, M.; Kresse, G. Accurate Quasiparticle Spectra from Self-Consistent GW Calculations with Vertex Corrections. *Phys. Rev. Lett.* **2007**, *99*, 246403.
- (14) Ethridge, E. C.; Fry, J. L.; Zaider, M. Quasiparticle spectra of trans-polyacetylene. *Phys. Rev. B* **1996**, *53*, 3662–3668.

- (15) van der Horst, J.-W.; Bobbert, P. A.; Michels, M. A. J.; Brocks, G.; Kelly, P. J. Ab Initio Calculation of the Electronic and Optical Excitations in Polythiophene: Effects of Intra- and Interchain Screening. *Phys. Rev. Lett.* **1999**, *83*, 4413–4416.
- (16) Rohlfing, M.; Louie, S. G. Optical Excitations in Conjugated Polymers. *Phys. Rev. Lett.* **1999**, *82*, 1959–1962.
- (17) Stan, A.; Dahlen, N. E.; van Leeuwen, R. Fully self-consistent GW calculations for atoms and molecules. *EPL* **2006**, *76*, 298–304.
- (18) Sai, N.; Tiago, M. L.; Chelikowsky, J. R.; Reboredo, F. A. Optical spectra and exchange-correlation effects in molecular crystals. *Phys. Rev. B* **2008**, *77*, 161306.
- (19) Ma, Y.; Rohlfing, M.; Molteni, C. Excited states of biological chromophores studied using many-body perturbation theory: Effects of resonant-antiresonant coupling and dynamical screening. *Phys. Rev. B* **2009**, *80*, 241405.
- (20) Rostgaard, C.; Jacobsen, K. W.; Thygesen, K. S. Fully self-consistent GW calculations for molecules. *Phys. Rev. B* **2010**, *81*, 085103.
- (21) Blase, X.; Attaccalite, C.; Olevano, V. First-principles *GW* calculations for fullerenes, porphyrins, phtalocyanine, and other molecules of interest for organic photovoltaic applications. *Phys. Rev. B* **2011**, *83*, 115103.
- (22) Faber, C.; Attaccalite, C.; Olevano, V.; Runge, E.; Blase, X. First-principles *GW* calculations for DNA and RNA nucleobases. *Phys. Rev. B* **2011**, *83*, 115123.
- (23) Faber, C.; Janssen, J. L.; Côté, M.; Runge, E.; Blase, X. Electron-phonon coupling in the C₆₀ fullerene within the many-body *GW* approach. *Phys. Rev. B* **2011**, *84*, 155104.
- (24) Foerster, D.; Koval, P.; Sánchez-Portal, D. An $O(N^3)$ implementation of Hedin’s *GW* approximation for molecules. *J. Chem. Phys.* **2011**, *135*, 074105.

- (25) Ke, S.-H. All-electron *GW* methods implemented in molecular orbital space: Ionization energy and electron affinity of conjugated molecules. *Phys. Rev. B* **2011**, *84*, 205415.
- (26) Baumeier, B.; Andrienko, D.; Rohlfing, M. Frenkel and Charge-Transfer Excitations in Donor–acceptor Complexes from Many-Body Green’s Functions Theory. *J. Chem. Theory Comput.* **2012**, *8*, 2790–2795, PMID: 26592120.
- (27) Körzdörfer, T.; Marom, N. Strategy for finding a reliable starting point for G_0W_0 demonstrated for molecules. *Phys. Rev. B* **2012**, *86*, 041110.
- (28) Bruneval, F.; Marques, M. A. L. Benchmarking the Starting Points of the *GW* Approximation for Molecules. *J. Chem. Theory Comput.* **2013**, *9*, 324–329, PMID: 26589035.
- (29) Pham, T. A.; Nguyen, H.-V.; Rocca, D.; Galli, G. *GW* calculations using the spectral decomposition of the dielectric matrix: Verification, validation, and comparison of methods. *Phys. Rev. B* **2013**, *87*, 155148.
- (30) van Setten, M. J.; Weigend, F.; Evers, F. The *GW*-Method for Quantum Chemistry Applications: Theory and Implementation. *J. Chem. Theory Comput.* **2013**, *9*, 232–246, PMID: 26589026.
- (31) Umari, P.; Giacomazzi, L.; De Angelis, F.; Pastore, M.; Baroni, S. Energy-level alignment in organic dye-sensitized TiO₂ from *GW* calculations. *J. Chem. Phys.* **2013**, *139*, 014709.
- (32) Cudazzo, P.; Gatti, M.; Rubio, A.; Sottile, F. Frenkel versus charge-transfer exciton dispersion in molecular crystals. *Phys. Rev. B* **2013**, *88*, 195152.
- (33) Lischner, J.; Sharifzadeh, S.; Deslippe, J.; Neaton, J. B.; Louie, S. G. Effects of self-consistency and plasmon-pole models on *GW* calculations for closed-shell molecules. *Phys. Rev. B* **2014**, *90*, 115130.

- (34) Koval, P.; Foerster, D.; Sánchez-Portal, D. Fully self-consistent *GW* and quasiparticle self-consistent *GW* for molecules. *Phys. Rev. B* **2014**, *89*, 155417.
- (35) Krause, K.; Harding, M. E.; Klopper, W. Coupled-cluster reference values for the GW27 and GW100 test sets for the assessment of *GW* methods. *Mol. Phys.* **2015**, *113*, 1952–1960.
- (36) van Setten, M. J.; Caruso, F.; Sharifzadeh, S.; Ren, X.; Scheffler, M.; Liu, F.; Lischner, J.; Lin, L.; Deslippe, J. R.; Louie, S. G.; Yang, C.; Weigend, F.; Neaton, J. B.; Evers, F.; Rinke, P. *GW*100: Benchmarking G_0W_0 for Molecular Systems. *J. Chem. Theory Comput.* **2015**, *11*, 5665–5687, PMID: 26642984.
- (37) Kaplan, F.; Harding, M. E.; Seiler, C.; Weigend, F.; Evers, F.; van Setten, M. J. Quasi-Particle Self-Consistent *GW* for Molecules. *J. Chem. Theory Comput.* **2016**, *12*, 2528–2541, PMID: 27168352.
- (38) Wilhelm, J.; Del Ben, M.; Hutter, J. *GW* in the Gaussian and Plane Waves Scheme with Application to Linear Acenes. *J. Chem. Theory Comput.* **2016**, *12*, 3623–3635, PMID: 27348184.
- (39) Rangel, T.; Hamed, S. M.; Bruneval, F.; Neaton, J. B. Evaluating the *GW* Approximation with CCSD(T) for Charged Excitations Across the Oligoacenes. *J. Chem. Theory Comput.* **2016**, *12*, 2834–2842, PMID: 27123935.
- (40) Scherpelz, P.; Govoni, M.; Hamada, I.; Galli, G. Implementation and Validation of Fully Relativistic *GW* Calculations: Spin–Orbit Coupling in Molecules, Nanocrystals, and Solids. *J. Chem. Theory Comput.* **2016**, *12*, 3523–3544, PMID: 27331614.
- (41) Knight, J. W.; Wang, X.; Gallandi, L.; Dolgounitcheva, O.; Ren, X.; Ortiz, J. V.; Rinke, P.; Körzdörfer, T.; Marom, N. Accurate Ionization Potentials and Electron Affinities of Acceptor Molecules III: A Benchmark of *GW* Methods. *J. Chem. Theory Comput.* **2016**, *12*, 615–626.

- (42) Vlček, V.; Rabani, E.; Neuhauser, D.; Baer, R. Stochastic GW Calculations for Molecules. *J. Chem. Theory Comput.* **2017**, *13*, 4997–5003, PMID: 28876912.
- (43) Maggio, E.; Liu, P.; van Setten, M. J.; Kresse, G. GW100: A Plane Wave Perspective for Small Molecules. *J. Chem. Theory Comput.* **2017**, *13*, 635–648, PMID: 28094981.
- (44) Maggio, E.; Kresse, G. GW Vertex Corrected Calculations for Molecular Systems. *J. Chem. Theory Comput.* **2017**, *13*, 4765–4778, PMID: 28873298.
- (45) Marom, N. Accurate description of the electronic structure of organic semiconductors by the GW methods. *J. Phys.: Cond. Matt.* **2017**, *29*, 103003.
- (46) Golze, D.; Wilhelm, J.; van Setten, M. J.; Rinke, P. Core-Level Binding Energies from GW: An Efficient Full-Frequency Approach within a Localized Basis. *J. Chem. Theory Comput.* **2018**, *14*, 4856–4869, PMID: 30092140.
- (47) Govoni, M.; Galli, G. GW100: Comparison of Methods and Accuracy of Results Obtained with the WEST Code. *J. Chem. Theory Comput.* **2018**, *14*, 1895–1909.
- (48) Vèril, M.; Romaniello, P.; Berger, J. A.; Loos, P.-F. Unphysical Discontinuities in GW Methods. *J. Chem. Theory Comput.* **2018**, *14*, 5220–5228, PMID: 30212627.
- (49) Wehner, J.; Brombacher, L.; Brown, J.; Junghans, C.; Çaylak, O.; Khalak, Y.; Madhikar, P.; Tirimbò, G.; Baumeier, B. Electronic Excitations in Complex Molecular Environments: Many-Body Green’s Functions Theory in VOTCA-XTP. *J. Chem. Theory Comput.* **2018**, *14*, 6253–6268, PMID: 30404449.
- (50) Holzer, C.; Klopper, W. Ionized, electron-attached, and excited states of molecular systems with spin–orbit coupling: Two-component GW and Bethe–Salpeter implementations. *J. Chem. Phys.* **2019**, *150*, 204116.
- (51) Bruneval, F. Assessment of the Linearized GW Density Matrix for Molecules. *J. Chem. Theory Comput.* **2019**, *15*, 4069–4078, PMID: 31194540.

- (52) Li, J.; Duchemin, I.; Roscioni, O. M.; Friederich, P.; Anderson, M.; Da Como, E.; Kociok-Köhn, G.; Wenzel, W.; Zannoni, C.; Beljonne, D.; Blase, X.; D’Avino, G. Host dependence of the electron affinity of molecular dopants. *Mater. Horiz.* **2019**, *6*, 107–114.
- (53) Koval, P.; Ljungberg, M. P.; Müller, M.; Sánchez-Portal, D. Toward Efficient *GW* Calculations Using Numerical Atomic Orbitals: Benchmarking and Application to Molecular Dynamics Simulations. *J. Chem. Theory Comput.* **2019**, *15*, 4564–4580, PMID: 31318555.
- (54) Bruneval, F.; Maliyov, I.; Lapointe, C.; Marinica, M.-C. Extrapolating Unconverged *GW* Energies up to the Complete Basis Set Limit with Linear Regression. *J. Chem. Theory Comput.* **2020**, *16*, 4399–4407, PMID: 32491851.
- (55) Loos, P.-F.; Pradines, B.; Scemama, A.; Giner, E.; Toulouse, J. Density-Based Basis-Set Incompleteness Correction for *GW* Methods. *J. Chem. Theory Comput.* **2020**, *16*, 1018–1028, PMID: 31891503.
- (56) Berger, J. A.; Loos, P.-F.; Romaniello, P. Potential Energy Surfaces without Unphysical Discontinuities: The Coulomb Hole Plus Screened Exchange Approach. *J. Chem. Theory Comput.* **2021**, *17*, 191–200, PMID: 33306908.
- (57) Whitten, J. L. Coulombic potential energy integrals and approximations. *J. Chem. Phys.* **1973**, *58*, 4496–4501.
- (58) Baerends, E.; Ellis, D.; Ros, P. Self-consistent molecular Hartree—Fock—Slater calculations I. The computational procedure. *Chem. Phys.* **1973**, *2*, 41 – 51.
- (59) Dunlap, B. I.; Connolly, J. W. D.; Sabin, J. R. On some approximations in applications of $X\alpha$ theory. *J. Chem. Phys.* **1979**, *71*, 3396–3402.

- (60) Vahtras, O.; Almlöf, J.; Feyereisen, M. Integral approximations for LCAO-SCF calculations. *Chem. Phys. Lett.* **1993**, *213*, 514 – 518.
- (61) Klopper, W.; Samson, C. C. M. Explicitly correlated second-order Møller–Plesset methods with auxiliary basis sets. *J. Chem. Phys.* **2002**, *116*, 6397–6410.
- (62) Ren, X.; Rinke, P.; Blum, V.; Wieferink, J.; Tkatchenko, A.; Sanfilippo, A.; Reuter, K.; Scheffler, M. Resolution-of-identity approach to Hartree-Fock, hybrid density functionals, RPA, MP2 and *GW* with numeric atom-centered orbital basis functions. *New J. Phys.* **2012**, *14*, 053020.
- (63) Duchemin, I.; Li, J.; Blase, X. Hybrid and Constrained Resolution-of-Identity Techniques for Coulomb Integrals. *J. Chem. Theory Comput.* **2017**, *13*, 1199–1208, PMID: 28094983.
- (64) Duchemin, I.; Deutsch, T.; Blase, X. Short-Range to Long-Range Charge-Transfer Excitations in the Zincbacteriochlorin-Bacteriochlorin Complex: A Bethe-Salpeter Study. *Phys. Rev. Lett.* **2012**, *109*, 167801.
- (65) Govoni, M.; Galli, G. Large Scale *GW* Calculations. *J. Chem. Theory Comput.* **2015**, *11*, 2680–2696, PMID: 26575564.
- (66) Li, J.; D’Avino, G.; Pershin, A.; Jacquemin, D.; Duchemin, I.; Beljonne, D.; Blase, X. Correlated electron-hole mechanism for molecular doping in organic semiconductors. *Phys. Rev. Materials* **2017**, *1*, 025602.
- (67) Ben, M. D.; da Jornada, F. H.; Canning, A.; Wichmann, N.; Raman, K.; Sasanka, R.; Yang, C.; Louie, S. G.; Deslippe, J. Large-scale *GW* calculations on pre-exascale HPC systems. *Comput. Phys. Commun.* **2019**, *235*, 187 – 195.
- (68) Rojas, H. N.; Godby, R. W.; Needs, R. J. Space-Time Method for Ab Initio Calculations.

- lations of Self-Energies and Dielectric Response Functions of Solids. *Phys. Rev. Lett.* **1995**, *74*, 1827–1830.
- (69) Neuhauser, D.; Rabani, E.; Baer, R. Expeditious Stochastic Calculation of Random-Phase Approximation Energies for Thousands of Electrons in Three Dimensions. *J. Phys. Chem. Lett.* **2013**, *4*, 1172–1176.
- (70) Liu, P.; Kaltak, M.; Klimeš, J.; Kresse, G. Cubic scaling *GW*: Towards fast quasiparticle calculations. *Phys. Rev. B* **2016**, *94*, 165109.
- (71) Wilhelm, J.; Golze, D.; Talirz, L.; Hutter, J.; Pignedoli, C. A. Toward *GW* Calculations on Thousands of Atoms. *J. Phys. Chem. Lett.* **2018**, *9*, 306–312, PMID: 29280376.
- (72) Gao, W.; Chelikowsky, J. R. Accelerating Time-Dependent Density Functional Theory and *GW* Calculations for Molecules and Nanoclusters with Symmetry Adapted Interpolative Separable Density Fitting. *J. Chem. Theory Comput.* **2020**, *16*, 2216–2223, PMID: 32074452.
- (73) Kim, M.; Martyna, G. J.; Ismail-Beigi, S. Complex-time shredded propagator method for large-scale *GW* calculations. *Phys. Rev. B* **2020**, *101*, 035139.
- (74) Kutepov, A. Self-consistent *GW* method: $O(N)$ algorithm for polarizability and self energy. *Comput. Phys. Commun.* **2020**, *257*, 107502.
- (75) Förster, A.; Visscher, L. Low-Order Scaling G_0W_0 by Pair Atomic Density Fitting. *J. Chem. Theory Comput.* **2020**, *16*, 7381–7399, PMID: 33174743.
- (76) Wilhelm, J.; Seewald, P.; Golze, D. Low-Scaling *GW* with Benchmark Accuracy and Application to Phosphorene Nanosheets. *J. Chem. Theory Comput.* **2021**, *17*, 1662–1677, PMID: 33621085.

- (77) Almlöf, J. Elimination of energy denominators in Møller-Plesset perturbation theory by a Laplace transform approach. *Chem. Phys. Lett.* **1991**, *181*, 319 – 320.
- (78) Häser, M.; Almlöf, J. Laplace transform techniques in Møller-Plesset perturbation theory. *J. Chem. Phys.* **1992**, *96*, 489–494.
- (79) Kaltak, M.; Klimeš, J.; Kresse, G. Cubic scaling algorithm for the random phase approximation: Self-interstitials and vacancies in Si. *Phys. Rev. B* **2014**, *90*, 054115.
- (80) Neese, F.; Wennmohs, F.; Hansen, A.; Becker, U. Efficient, approximate and parallel Hartree–Fock and hybrid DFT calculations. A ‘chain-of-spheres’ algorithm for the Hartree–Fock exchange. *Chem. Phys.* **2009**, *356*, 98 – 109.
- (81) Izsák, R.; Neese, F. An overlap fitted chain of spheres exchange method. *J. Chem. Phys.* **2011**, *135*, 144105.
- (82) Izsák, R.; Neese, F.; Klopper, W. Robust fitting techniques in the chain of spheres approximation to the Fock exchange: The role of the complementary space. *J. Chem. Phys.* **2013**, *139*, 094111.
- (83) Parrish, R. M.; Hohenstein, E. G.; Martínez, T. J.; Sherrill, C. D. Tensor hypercontraction. II. Least-squares renormalization. *J. Chem. Phys.* **2012**, *137*, 224106.
- (84) Hohenstein, E. G.; Parrish, R. M.; Sherrill, C. D.; Martínez, T. J. Communication: Tensor hypercontraction. III. Least-squares tensor hypercontraction for the determination of correlated wavefunctions. *J. Chem. Phys.* **2012**, *137*, 221101.
- (85) Kokkila Schumacher, S. I. L.; Hohenstein, E. G.; Parrish, R. M.; Wang, L.-P.; Martínez, T. J. Tensor Hypercontraction Second-Order Møller–Plesset Perturbation Theory: Grid Optimization and Reaction Energies. *J. Chem. Theory Comput.* **2015**, *11*, 3042–3052, PMID: 26575741.

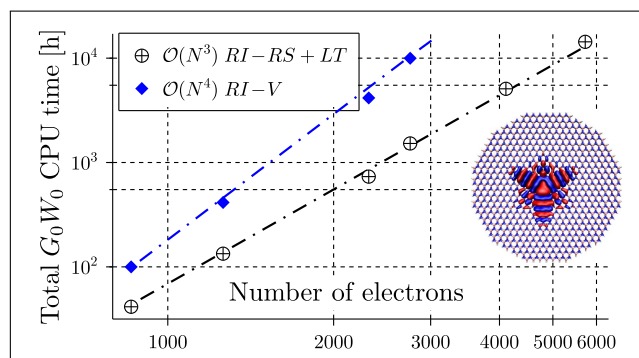
- (86) Lu, J.; Ying, L. Compression of the electron repulsion integral tensor in tensor hypercontraction format with cubic scaling cost. *J. Comput. Phys.* **2015**, *302*, 329 – 335.
- (87) Lu, J.; Ying, L. Fast algorithm for periodic density fitting for Bloch waves. *Ann. Math. Sci. Appl.* **2016**, *1*, 321 – 339.
- (88) Hu, W.; Lin, L.; Yang, C. Interpolative Separable Density Fitting Decomposition for Accelerating Hybrid Density Functional Calculations with Applications to Defects in Silicon. *J. Chem. Theory Comput.* **2017**, *13*, 5420–5431, PMID: 28960982.
- (89) Dong, K.; Hu, W.; Lin, L. Interpolative Separable Density Fitting through Centroidal Voronoi Tessellation with Applications to Hybrid Functional Electronic Structure Calculations. *J. Chem. Theory Comput.* **2018**, *14*, 1311–1320, PMID: 29370521.
- (90) Hu, W.; Shao, M.; Cepellotti, A.; da Jornada, F. H.; Lin, L.; Thicke, K.; Yang, C.; Louie, S. In *Lect. Notes Comput. Sci.*; et al. (eds) Computational Science – ICCS 2018. ICCS 2018 Springer, S. Y., Ed.; 2018; Vol. 10861; Chapter Accelerating Optical Absorption Spectra and Exciton Energy Computation via Interpolative Separable Density Fitting.
- (91) Hu, W.; Liu, J.; Li, Y.; Ding, Z.; Yang, C.; Yang, J. Accelerating Excitation Energy Computation in Molecules and Solids within Linear-Response Time-Dependent Density Functional Theory via Interpolative Separable Density Fitting Decomposition. *J. Chem. Theory Comput.* **2020**, *16*, 964–973, PMID: 31899646.
- (92) Malone, F. D.; Zhang, S.; Morales, M. A. Overcoming the Memory Bottleneck in Auxiliary Field Quantum Monte Carlo Simulations with Interpolative Separable Density Fitting. *J. Chem. Theory Comput.* **2019**, *15*, 256–264.
- (93) Lee, J.; Lin, L.; Head-Gordon, M. Systematically Improvable Tensor Hypercontraction: Interpolative Separable Density-Fitting for Molecules Applied to Exact Exchange,

- Second- and Third-Order Møller–Plesset Perturbation Theory. *J. Chem. Theory Comput.* **2020**, *16*, 243–263, PMID: 31794667.
- (94) Duchemin, I.; Blase, X. Separable resolution-of-the-identity with all-electron Gaussian bases: Application to cubic-scaling RPA. *J. Chem. Phys.* **2019**, *150*, 174120.
- (95) Weigend, F.; Köhn, A.; Hättig, C. Efficient use of the correlation consistent basis sets in resolution of the identity MP2 calculations. *J. Chem. Phys.* **2002**, *116*, 3175–3183.
- (96) Weigend, F.; Häser, M.; Patzelt, H.; Ahlrichs, R. RI-MP2: optimized auxiliary basis sets and demonstration of efficiency. *Chem. Phys. Lett.* **1998**, *294*, 143 – 152.
- (97) Friedrich, C. Tetrahedron integration method for strongly varying functions: Application to the *GT* self-energy. *Phys. Rev. B* **2019**, *100*, 075142.
- (98) Duchemin, I.; Blase, X. Robust Analytic-Continuation Approach to Many-Body GW Calculations. *J. Chem. Theory Comput.* **2020**, *16*, 1742–1756, PMID: 32023052.
- (99) Becke, A. D. A multicenter numerical integration scheme for polyatomic molecules. *J. Chem. Phys.* **1988**, *88*, 2547–2553.
- (100) Kaltak, M.; Klimeš, J.; Kresse, G. Low Scaling Algorithms for the Random Phase Approximation: Imaginary Time and Laplace Transformations. *J. Chem. Theory Comput.* **2014**, *10*, 2498–2507, PMID: 26580770.
- (101) Caruso, F.; Dauth, M.; van Setten, M. J.; Rinke, P. Benchmark of *GW* Approaches for the *GW100* Test Set. *J. Chem. Theory Comput.* **2016**, *12*, 5076–5087, PMID: 27631585.
- (102) Rebolini, E.; Izsák, R.; Reine, S. S.; Helgaker, T.; Pedersen, T. B. Comparison of Three Efficient Approximate Exact-Exchange Algorithms: The Chain-of-Spheres Algorithm, Pair-Atomic Resolution-of-the-Identity Method, and Auxiliary Density Matrix Method. *J. Chem. Theory Comput.* **2016**, *12*, 3514–3522, PMID: 27224306.

- (103) Matthews, D. A. Improved Grid Optimization and Fitting in Least Squares Tensor Hypercontraction. *J. Chem. Theory Comput.* **2020**, *16*, 1382–1385, PMID: 32004002.
- (104) Tran, T. T.; Bray, K.; Ford, M. J.; Toth, M.; Aharonovich, I. Quantum emission from hexagonal boron nitride monolayers. *Nat. Nanotechnol.* **2015**, *11*, 37.
- (105) Tran, T. T.; Zachreson, C.; Berhane, A. M.; Bray, K.; Sandstrom, R. G.; Li, L. H.; Taniguchi, T.; Watanabe, K.; Aharonovich, I.; Toth, M. Quantum Emission from Defects in Single-Crystalline Hexagonal Boron Nitride. *Phys. Rev. Appl.* **2016**, *5*, 034005.
- (106) Martínez, L. J.; Pelini, T.; Waselowski, V.; Maze, J. R.; Gil, B.; Cassabois, G.; Jacques, V. Efficient single photon emission from a high-purity hexagonal boron nitride crystal. *Phys. Rev. B* **2016**, *94*, 121405.
- (107) Bourrellier, R.; Meuret, S.; Tararan, A.; Stéphan, O.; Kociak, M.; Tizei, L. H. G.; Zobelli, A. Bright UV Single Photon Emission at Point Defects in h-BN. *Nano Lett.* **2016**, *16*, 4317–4321, PMID: 27299915.
- (108) Jungwirth, N. R.; Fuchs, G. D. Optical Absorption and Emission Mechanisms of Single Defects in Hexagonal Boron Nitride. *Phys. Rev. Lett.* **2017**, *119*, 057401.
- (109) Wu, F.; Galatas, A.; Sundararaman, R.; Rocca, D.; Ping, Y. First-principles engineering of charged defects for two-dimensional quantum technologies. *Phys. Rev. Mater.* **2017**, *1*, 071001.
- (110) Attaccalite, C.; Bockstedte, M.; Marini, A.; Rubio, A.; Wirtz, L. Coupling of excitons and defect states in boron-nitride nanostructures. *Phys. Rev. B* **2011**, *83*, 144115.
- (111) Krishnan, R.; Binkley, J. S.; Seeger, R.; Pople, J. A. Self-consistent molecular orbital methods. XX. A basis set for correlated wave functions. *J. Chem. Phys.* **1980**, *72*, 650–654.

- (112) See e.g. Ref. ? in the case of molecular thin films.
- (113) Weigend, F. Accurate Coulomb-fitting basis sets for H to Rn. *Phys. Chem. Chem. Phys.* **2006**, *8*, 1057–1065.
- (114) Schindlmayr, A. Decay properties of the one-particle Green function in real space and imaginary time. *Phys. Rev. B* **2000**, *62*, 12573–12576.

Graphical TOC Entry



Scaling with system size for 6-311G* G_0W_0 calculations performed with the cubic scaling real-space Laplace transform scheme (RI-RS+LT) as compared to the quartic scaling traditional Coulomb fitting (RI-V) approach for a family of defected boron-nitride flakes.

Supporting Information for:

Cubic-scaling all-electron GW calculations with a separable density-fitting space-time approach

Ivan Duchemin^{*,†} and Xavier Blase[‡]

[†]*Univ. Grenoble Alpes, CEA, IRIG-MEM-L_Sim, 38054 Grenoble, France*

[‡]*Univ. Grenoble Alpes, CNRS, Inst NEEL, F-38042 Grenoble, France*

E-mail: ivan.duchemin@cea.fr

1 Details of the def2-TZVP G_0W_0 calculations on the $GW100$ test set.

Table S1: HOMO and LUMO energies at the def2-TZVP $G_0W_0@PBE0$ level for the $GW100$ molecular test set.^{S1} The standard Coulomb-fitting scheme (RI-V) performed with the def2-TZVP-RI auxiliary basis set^{S2} is compared to the present real-space Laplace-transform (RI-RS) calculations. Negative and positive maximum errors, the mean absolute (MAE) and mean signed (MSE) errors are indicated in meV. Values leading to the largest error are in bold.

	HOMO		LUMO	
	RI-V [eV]	RI-RS [eV]	RI-V [eV]	RI-RS [eV]
Acetaldehyde	-9.8658	-9.8654	1.7301	1.7299
Acetylene	-11.1190	-11.1189	3.4524	3.4524
Adenine	-8.0278	-8.0277	1.0619	1.0617
Aluminumtrifluoride	-14.7007	-14.7006	0.6740	0.6739
Amonia	-10.4839	-10.4837	3.0423	3.0423
Aniline	-7.6936	-7.6934	1.6764	1.6762
Argon	-15.1917	-15.1917	14.7162	14.7162
Arsenicdimer	-9.4097	-9.4093	-0.3135	-0.3136

Continued on next page

Table S1 – GW100 G_0W_0 @PBE0 data, continued from previous page

	HOMO		LUMO	
	RI-V [eV]	RI-RS [eV]	RI-V [eV]	RI-RS [eV]
Arsine	-10.1110	-10.1111	3.0944	3.0946
Benzene	-9.0143	-9.0140	1.5996	1.5997
Berylliummonoxide	-12.9594	-12.9595	-11.6442	-11.6442
Borane	-13.0064	-13.0064	0.4548	0.4547
Boronnitride	-11.3781	-11.3782	-3.5945	-3.5945
Bromine	-10.1504	-10.1495	-0.8253	-0.8247
Buthane	-11.5753	-11.5754	2.9304	2.9302
Carbondioxide	-13.4373	-13.4371	2.9403	2.9403
Carbondisulfide	-9.7561	-9.7562	0.2424	0.2424
Carbonmonoxide	-13.9578	-13.9576	1.0780	1.0779
Carboxyselenide	-10.1634	-10.1633	1.3249	1.3248
Carboxysulfide	-10.9454	-10.9453	1.7287	1.7287
Carbontetrabromide	-9.9729	-9.9719	-0.4853	-0.4847
Carbontetrachloride	-11.1414	-11.1409	0.7781	0.7780
Carbontetrafluoride	-15.7426	-15.7419	4.9648	4.9653
Chlorine	-11.1315	-11.1316	-0.1991	-0.1991
Coppercyanide	-10.0069	-10.0052	-1.0328	-1.0327
Copperdimer	-7.3478	-7.3479	-0.3626	-0.3624
Cyclooctatetraene	-8.0888	-8.0886	0.5793	0.5791
Cyclopentadiene	-8.3697	-8.3699	1.5707	1.5707
Cyclopropane	-10.6135	-10.6138	3.5310	3.5311
Cytosine	-8.4546	-8.4546	0.8030	0.8029
Diborane6	-11.9952	-11.9951	1.2461	1.2460
Dipotassium	-3.9849	-3.9849	-0.4377	-0.4377
Disilane	-10.3480	-10.3480	2.2701	2.2702
Ethane	-12.4466	-12.4468	3.1998	3.1998
Ethanol	-10.3587	-10.3592	2.9515	2.9515
Ethoxyethane	-9.5363	-9.5364	3.0017	3.0014
Ethylbenzene	-8.5805	-8.5805	1.5685	1.5687
Ethylene	-10.3456	-10.3455	2.5831	2.5831
Fluorine	-15.3320	-15.3322	0.1373	0.1372
Fluoroborane	-10.7671	-10.7671	1.5093	1.5092
Formaldehyde	-10.5488	-10.5487	1.5744	1.5745
Formic Acid	-11.0648	-11.0647	2.5916	2.5915
Galliummonochloride	-9.5438	-9.5438	0.3533	0.3532
Germane	-12.1362	-12.1362	3.2973	3.2973
Guanine	-7.7447	-7.7449	1.3749	1.3750
Helium	-23.7926	-23.7926	22.2760	22.2760
Hexafluorobenzene	-9.6562	-9.6563	0.9102	0.9101
Hydrazene	-9.4265	-9.4264	2.6692	2.6691

Continued on next page

Table S1 – GW100 G_0W_0 @PBE0 data, continued from previous page

	HOMO		LUMO	
	RI-V [eV]	RI-RS [eV]	RI-V [eV]	RI-RS [eV]
Hydrogen	-15.9491	-15.9491	4.4635	4.4635
Hydrogenazide	-10.4807	-10.4811	1.8777	1.8776
Hydrogenchloride	-12.2631	-12.2632	2.8900	2.8900
Hydrogencyanide	-13.3566	-13.3569	3.1549	3.1550
Hydrogenfluoride	-15.5491	-15.5491	3.2673	3.2673
Hydrogenperoxide	-11.2224	-11.2222	3.1763	3.1764
Hydrogensulfide	-10.0084	-10.0084	3.2376	3.2376
Krypton	-13.4876	-13.4865	10.4118	10.4122
Lithiumdimer	-5.0389	-5.0389	-0.1772	-0.1771
Lithiumfluoride	-10.4604	-10.4603	0.1233	0.1232
Lithiumhydride	-7.3073	-7.3072	0.1841	0.1841
Magnesiumchloride	-11.2469	-11.2469	-0.1141	-0.1142
Magnesiumfluoride	-12.9920	-12.9921	0.0598	0.0599
Magnesiummonoxide	-7.3227	-7.3226	-1.5708	-1.5708
Methane	-14.0449	-14.0452	3.5594	3.5594
Methanol	-10.7266	-10.7268	3.1640	3.1639
Neon	-20.7658	-20.7657	20.8885	20.8885
Nitrogen	-15.2455	-15.2455	2.9042	2.9041
Ozon	-12.3624	-12.3620	-1.8652	-1.8654
Pentasilane	-8.9797	-8.9796	0.7289	0.7289
Phenol	-8.3968	-8.3966	1.4663	1.4663
Phenol (v2)	-8.2916	-8.2912	1.5195	1.5196
Phosphine	-10.2794	-10.2793	3.1459	3.1460
Phosphorusdimer	-10.1723	-10.1723	-0.2715	-0.2715
Phosphorusmononitride	-11.4976	-11.4975	0.2857	0.2857
Potassiumbromide	-7.6723	-7.6718	-0.2585	-0.2584
Potassiumhydride	-5.4022	-5.4022	0.0491	0.0492
Propane	-11.8751	-11.8750	3.0092	3.0093
Pyridine	-9.3883	-9.3877	1.0332	1.0330
Silane	-12.4656	-12.4657	3.2217	3.2217
Sodiumchloride	-8.5723	-8.5725	-0.4087	-0.4087
Sodiumdimer	-4.9076	-4.9076	-0.3663	-0.3663
Sodiumhexamer	-4.2910	-4.2910	-0.6794	-0.6794
Sodiumtetramer	-4.1678	-4.1677	-0.7052	-0.7052
Sulferdioxide	-12.0048	-12.0045	-0.4411	-0.4412
Sulfertetrafluoride	-12.2741	-12.2753	0.9815	0.9813
Tetracarbon	-11.0137	-11.0139	-2.5154	-2.5154
Thymine	-8.8343	-8.8341	0.5947	0.5946
Titaniumfluoride	-14.6675	-14.6670	-0.2178	-0.2178
Tuloene	-8.6321	-8.6316	1.5334	1.5333

Continued on next page

Table S1 – GW100 G_0W_0 @PBE0 data, continued from previous page

	HOMO		LUMO	
	RI-V [eV]	RI-RS [eV]	RI-V [eV]	RI-RS [eV]
Uracil	-9.2341	-9.2340	0.5442	0.5440
Urea	-9.6647	-9.6650	2.4063	2.4063
Vynilbromide	-8.9477	-8.9475	1.9401	1.9401
Vynilbromidev2	-9.4866	-9.4861	1.8184	1.8183
Vynilchloride	-9.7883	-9.7883	2.0109	2.0108
Vynilfluoride	-10.2372	-10.2377	2.7246	2.7247
Water	-12.1646	-12.1646	3.0779	3.0779
Max. err.	+1.67 meV / -1.16 meV		+0.66 meV / -0.30 meV	
MAE	0.21 meV		0.09 meV	
MSE	0.08 meV		0.001 meV	

2 Timings for the 6-311G* G_0W_0 @PBE0 calculations

We present in Table S2 additional details on the size, timing (walltime) and number of cores used concerning the defected h-BN systems. Calculations have been performed on 128-cores 2.6 GHz AMD Rome nodes with 1.85 Gb/core. For consistency between different systems, all calculations used fully filled nodes. Notice that real-space Laplace-transform (RI-RS+LT) calculations required much less cores than the standard RI-V scheme as the signature of reduced memory requirements.

Table S2: Number of B,C,N and H atoms, number of electrons, number of cores and timings in hh:mm:ss (walltime) for the 6-311G* G_0W_0 @PBE0 calculations on defected hexagonal boron-nitride flakes. The memory indicated represent the maximum memory available for the run.

$N_{B/C/N}$	N_H	N_{el}	N_{CPU}	RI-V		RI-RS+LT		
				walltime	mem.(Tb)	N_{CPU}	walltime	mem.(Tb)
137	30	852	384	00:15:37	0.72	128	00:19:26	0.24
203	36	1254	768	00:32:21	1.44	256	00:31:21	0.48
371	48	2274	3072	01:21:12	5.76	640	01:08:41	1.20
448	54	2742	6144	01:37:25	11.52	1152	01:19:18	2.16
674	65	4108	23040	02:46:32	43.20	2560	01:59:11	4.80
941	78	5724	–	–	–	5120	02:48:00	9.60

We further give the total CPU time associated with the main cubic-scaling operations (Fig. S1 and Table S3), namely the construction of the grid weights $M_{\mu,k}$ (RI setup), the

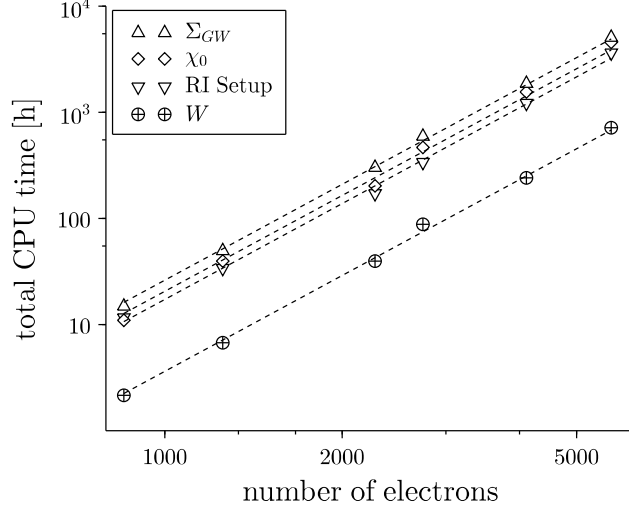


Figure S1: Scaling behavior for the 4 principal steps of our cubic-scaling G_0W_0 implementation. Dashed lines are guides for the eyes using an exact cubic behavior (slope equal to 3).

construction of the independent-electron susceptibilities (χ_0), the inversion of the Dyson equation to obtain the screened Coulomb potential (W), and finally the evaluation of the self-energy (Σ^{GW}). Taking the largest system, for which the 6-311G* space-time G_0W_0 calculation represents a total CPU time of about 14336 hours, the sum of these 4 steps amounts to 13984 hours, namely 98% of the total. For this largest flake, the RI set-up represents about 25% and the χ_0 calculations about 32% of the total CPU time.

Table S3: Number of atoms, electrons, cores and timings in hh:mm (total CPU time) for the principal computational steps of the 6-311G* RI-RS+LT G_0W_0 @PBE0 calculations.

$N_{B/C/N}$	N_H	N_{el}	N_{CPU}	total CPU time			
				RI setup	χ_0	W	Σ_{GW}
137	30	852	128	11:37	10:58	2:09	14:52
203	36	1254	256	33:56	39:40	6:45	49:31
371	48	2274	640	171:42	202:50	39:37	301:34
448	54	2742	1152	338:16	466:55	88:04	592:49
674	65	4108	2560	1219:20	1555:57	241:13	1866:17
941	78	5724	5120	3633:19	4564:49	715:42	5070:11

References

- [S1] van Setten, M. J.; Caruso, F.; Sharifzadeh, S.; Ren, X.; Scheffler, M.; Liu, F.; Lischner, J.; Lin, L.; Deslippe, J. R.; Louie, S. G.; Yang, C.; Weigend, F.; Neaton, J. B.; Evers, F.; Rinke, P. *GW100: Benchmarking G_0W_0 for Molecular Systems*. *J. Chem. Theory Comput.* **2015**, *11*, 5665–5687, PMID: 26642984.
- [S2] Weigend, F.; Häser, M.; Patzelt, H.; Ahlrichs, R. RI-MP2: optimized auxiliary basis sets and demonstration of efficiency. *Chem. Phys. Lett.* **1998**, *294*, 143 – 152.